Applied Catalysis B: Environmental 267 (2020) 118727

Contents lists available at ScienceDirect

Applied Catalysis B: Environmental

journal homepage: www.elsevier.com/locate/apcatb

Morphing $Mn_{core}@Pt_{shell}$ nanoparticles: Effects of core structure on the ORR performance of Pt shell

Md. Abdul Matin[a], Junsu Lee[b], Gwan Woo Kim[b], Hyun-Uk Park[a], Byeong Jun Cha[a], Sarvjit Shastri[c], Gunn Kim[b], Young-Dok Kim[a], Young-Uk Kwon[a,d,*], Valeri Petkov[e,**]

[a] Department of Chemistry, Sungkyunkwan University, Suwon, 16419, South Korea
[b] Department of Physics and Graphene Research Institute, Sejong University, Seoul, 05006, South Korea
[c] X-ray Science Division, Advanced Photon Source, Argonne National Laboratory, Argonne, IL, 60439, United States
[d] School of Material Science Engineering, Tianjin Polytechnic University, Tianjin, 300387, China
[e] Department of Physics, Central Michigan University, Mt. Pleasant, MI, 48859, United States

ARTICLE INFO

Keywords:
Platinum
Manganese
Core-shell nanoparticle
Electrocatalysis
Oxygen reduction reaction

ABSTRACT

Currently, the catalysts performance for the oxygen reduction reaction (ORR) is limited by two major factors, their price and the scaling relationship, i.e. constant offset, between the binding energy of reactants and reaction intermediates. Here we show that both limitations may be eased by using nanoparticle catalysts composed of a core of earth-abundant Mn and Pt shell of two atomic layers. The unusual atomic-structure of Mn core renders the distribution of coordination numbers and related atomic-level stresses on the Pt shell very broad in comparison to pure Pt particles. This increases the chances of nearby sites on the shell to affect each other's activity such that the dissociative absorption of molecular oxygen is facilitated without correspondingly increasing the binding strength of reaction intermediates, thereby promoting the ORR kinetics. Our findings introduce the concept of structural flexibility of the 3*d*-metal core and 5*d*-Pt shell as a strategy for catalysis performance.

1. Introduction

The progress of fuel cell technologies depends critically on the improvement of catalysts for the sluggish chemical reactions driving cells' operation, such as the oxygen reduction reaction (ORR). Despite the sustained research effort to find ORR catalysts free of expensive Pt [1], as of today, only Pt-based catalysts are found to approach the requirements for high activity and durability imposed by practical applications [2–6]. This has prompted researchers to explore sophisticated nanostructures, such as 3*d*-transition metal (TM) core and Pt shell (TM@Pt) nanoparticles (NPs), as superior alternatives to pure Pt NPs in terms of both affordability and activity. The current understanding is that the improved activity arises from specific interactions between the TM and Pt atoms, including charge transfer and optimization of atomic-level stresses [7–17]. Among others, Co@Pt [18,19] and Ni@Pt [20,21] NPs have emerged as particularly promising catalysts for ORR. More recent studies though have shown that enhancement in ORR activity and stability can also be achieved using other elements on the Periodic Table [22].

While most of late 3*d*-TMs have been explored as substitutes for face-centered-cubic (fcc) Pt, peculiarly, some middle and early 3d-TMs possessing a non-fcc type structure, such as body-centered-cubic (bcc) Mn and V, have been given little attention. As for Mn, there have been only a few reports on Mn-Pt nanoalloys [8,23,24], but not a single study has been reported on the synthesis of Mn@Pt NPs let alone the effect of Mn on the catalysis performance of Pt. One of the reasons may be traced back to the theoretical prediction of Stamenkovic et al. on the effects of TMs on the electronic structure of Pt, which sparked the present interest in Pt-TM catalysts. The prediction envisages a volcano-type dependence of the ORR activity of Pt_3TM alloys as a function of the atomic number of TMs, showing a peak for Co. According to the prediction, Mn would be one of the least effective TMs for producing cost-efficient and improved Pt-based catalysts for ORR [25]. Another likely reason is the difficult synthesis of small clusters of Mn^0 species, which are considered to be the first step in producing Mn@Pt NPs. The difficulty stems from the fact that, when compared with other 3d-TMs, Mn has a rather high oxidation potential [26]

By employing a single step sonochemical reaction, here we synthesize three samples of Mn@Pt NPs with a size of about 3 nm wherein the diameter of Mn core is so adjusted that Pt shell is about 1, 1.5 and 2

* Corresponding author at: Department of Chemistry, Sungkyunkwan University, Suwon, 16419, South Korea.
** Corresponding author.
E-mail addresses: ywkwon@skku.edu (Y.-U. Kwon), petko1vg@cmich.edu (V. Petkov).

https://doi.org/10.1016/j.apcatb.2020.118727
Received 17 July 2019; Received in revised form 29 January 2020; Accepted 3 February 2020
Available online 04 February 2020
0926-3373/

layers thick. Electrocatalytic measurements show that the activity of the NPs for ORR is 14–16 times higher than that exhibited by corresponding pure Pt NPs. The atomic-scale structure of Mn@Pt NPs is determined by resonant high-energy x-ray diffraction (HE-XRD) coupled to atomic pair distribution function (PDF) analysis and 3D computer modeling. From the coordinates of atoms in the structure models, the distribution of surface Pt-Pt bonding distances and coordination numbers for the NPs are obtained and compared with the electrocatalytic data side by side. The comparison shows that the coordination environment of surface Pt sites and site-specific atomic level stresses are highly diverse and, furthermore, evolve irregularly with the thickness of Pt shell. Furthermore, the cores morph from a less densely packed and relatively well-ordered to a more densely packed and less ordered bcc-type atomic configuration with the increase in the thickness of fcc Pt shell. Concurrently, the shell becomes more strained, and uneven, endowing the NPs with a superb catalytic activity for ORR. Thus, NPs composed of a non-fcc TM core with a flexible atomic structure and thin fcc-Pt shell appear to be very promising as catalysts for ORR. In line with our prior studies [27], the findings presented here challenge the conventional perceptions on the interaction between the core and shell of TM@Pt NPs in determining their electrocatalytic activity. Hence, they are likely to inspire further efforts to explore earth-abundant early and middle 3d-TMs as a component of catalysts for ORR and other reactions of utmost technological importance.

2. Experimental

2.1. Materials

Platinum (II) acetylacetonate ($Pt(acac)_2$, 97 %), Manganese (II) acetylacetonate ($Mn(acac)_2$, 97 %), perchloric acid (70 %), and Nafion solution (5 wt.%) were purchased from Aldrich. A commercial Pt/C (37.7 %, average diameter 2.6 nm) electrocatalyst was obtained from TKK. Ketjen Black, a type of porous carbon, was donated from Samsung Advanced Institute of Technology. Ethylene glycol (EG, 99.9 %) and ethanol (99.9 %) were purchased from Samchun Pure Chemical Co. Filter papers were purchased from Whatman Int. Ltd. Ultrapure water (Millipore, 18.2 MΩ cm) was used throughout the work.

2.2. Synthesis of Mn@Pt core-shell NPs

Mn@Pt NPs were prepared through one-step sonochemical reactions. Measured amounts of $Pt(acac)_2$, $Mn(acac)_2$, and carbon support (loading amounts are detailed in Table S1) were added to a three-necked flask containing EG (30 mL), which had been bubbled with pure Ar for 45 min prior to the addition to expel any dissolved reactive gases such as oxygen. Ultrasound with a 30 % amplitude from a 500 kW ultrasound generator (Sonic and Materials, VC-500, 20 kHz with a 13 mm solid probe) was applied for 3 h under an Ar-ambient. The blackish slurry was filtered, washed with ethanol, and then dried under vacuum for 12 h at room temperature.

2.3. Characterization techniques

X-ray diffraction (XRD) patterns of the samples were recorded with a powder X-ray diffractometer (DC/Max 2000, Rigaku, Cu K_α, (λ = 1.54056 Å)). The shape and size of the NPs were studied with a transmission electron microscope (TEM, JEOL, JE-3011, 300 kV). A very small amount of each sample was dispersed in ethanol with a sonicator. Then, several drops of the dispersed solution were deposited onto a carbon-coated Cu-grid, followed by drying in air. An energy dispersive X-ray spectroscopy (EDS) probe attached to a scanning TEM (JEOL, JEM-ARM 200F Atomic Resolution Analytical Microscope) was used to determine the compositions of the individual NPs in the samples. For the elemental distribution profiles, the microscope was operated at 300 kV in the high-angle dark field (HAADF) mode. The compositions are also confirmed by atomic emission spectroscopy. A fixed amount of each sample was dissolved in an aqua regia at ~100 °C for 4h and the resulting solutions were diluted with distilled water. The carbon support was separated from the solution using a syringe filter. Then, the solutions were analyzed by an inductively coupled plasma-atomic emission spectroscopy (ICP-AES, OPTIMA 4300DV PerkinElmer). Each sample was measured three times and the averaged data are presented here. X-ray photoelectron spectroscopy (XPS, ESCA 2000, VG Microtech.) was conducted with a monochromatic Al Kα source (1446.6 eV) to investigate the electronic state of Pt in the samples. The reported binding energies (BEs) from XPS are calibrated with respect to C 1s at 284.6 eV.

2.4. Resonant high-energy x-ray diffraction experiments

Resonant high-energy synchrotron XRD experiments were carried out at the 1-ID beamline of the Advanced Photon Source, Argonne. Two sets of HE-XRD patterns for each of Mn@xPt NPs were obtained using x-rays of two different energies. One of the sets was obtained using x-rays with energy of 78.370 keV, which is 25 eV below the K absorption edge of Pt. The other set of patterns was obtained using x-rays with energy of 78.070 keV, which is 325 eV below the K absorption edge of Pt. The patterns were processed as explained in the Supplementary Materials (SM) and reduced to atomic PDFs. The PDFs are shown in Fig. 1.

2.5. Density functional theory calculations

The catalytic activity of the NPs for ORR was evaluated by density functional theory (DFT) using the Vienna ab initio simulation package (VASP). In the calculations, spin polarization was taken into account. To describe the valence electrons, projector augmented wave potentials were used. For the exchange-correlation functional, the generalized gradient approximation of Perdue-Burke-Emzerhof was used [28]. Electronic wave functions were expanded into plane waves, and the cutoff of the kinetic energy was set to 500 eV. In the Brillouin-zone integration, the 4 × 4 × 1 Γ-centered Monkhorst-Pack sampling was employed. In the hexagonal unit cell, the cell parameters a and c were 7.71 Å and 20.00 Å, respectively. We considered the (111) surfaces for Mn and Pt fcc structures to mimic the Mn@Pt NPs, and computed the adsorption energies of a hydrogen (or an oxygen) atom on 1 ML (or 2 ML) platinum layers on top of a 4 atomic layers thick slab of Mn atoms. For each case, three symmetric adsorption sites, ontop, hollow, and bridge, were considered.

2.6. Electrochemical measurements

Electrochemical studies of Mn@Pt catalysts were performed on electrodes fabricated on a rotating disc electrode (RDE, Autolab). A commercial Pt/C was used as a reference. The glassy carbon (GC; d = 3.0 mm, area = 0.0707 cm^2) electrode of RDE was polished with an Al_2O_3 paste on a polishing cloth for ~10 s, and then rinsed with distilled water. 5 mg of a sample was dispersed in 2.5 g of distilled water by a sonicator until a dark homogeneous dispersion was produced. 5 μL of the dispersion was dropped on the surface of GC using a calibrated micropipette and let to dry out in air. In order to protect the electrode material from disintegrating, 5 μL of a 0.05 wt. % Nafion solution was applied over its surface.

The electrochemical properties were evaluated using a potentiostat (Ivium Compactstat, Ivium Technology) and a standard three-electrode electrochemical cell consisting of a Ag/AgCl (in 3 M KCl) reference electrode, a RDE working electrode, and a Pt-mesh counter electrode. Prior to each measurement, N_2 gas was bubbled through the electrolyte for 45 min in order to expel O_2. Furthermore, to remove any organic species, the working electrode was electrochemically cleaned in the potential range from 0.3 to 1.1 V with a scan rate 500 mV s^{-1} for 100 cycles. Cyclic voltammograms (CVs) were measured in a 0.1 M $HClO_4$

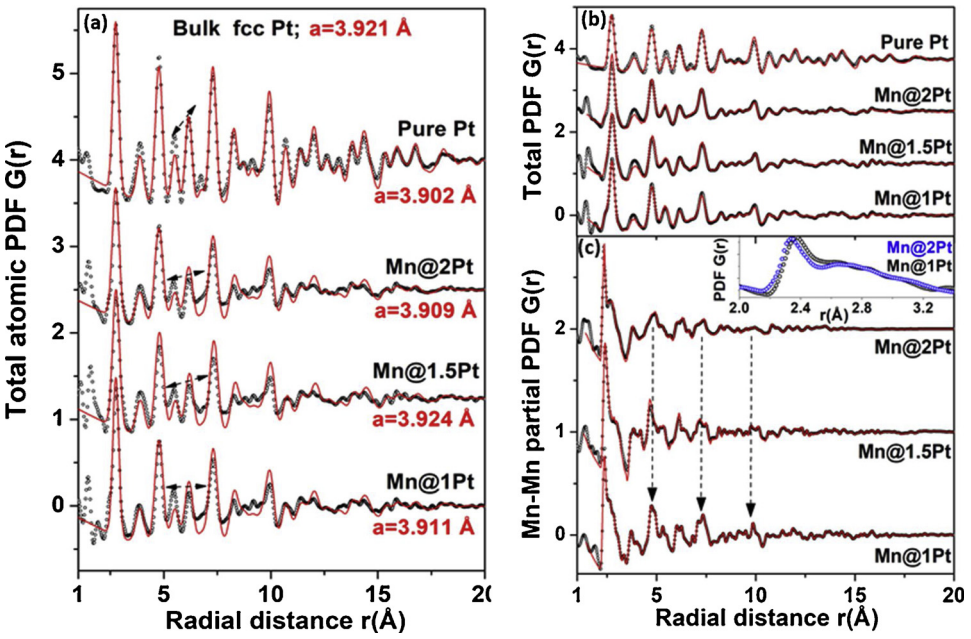

Fig. 1. (a) Experimental (symbols) and computed (red line) total atomic PDFs for pure Pt and Mn@xPt NPs. The computed PDFs are based on an fcc-lattice type model. The refined "fcc-lattice" parameters are show for each data set. Arrows emphasize inconsistencies between the experimental and fcc-model computed data. **(b)** RMC fits (red lines) to the experimental (symbols) total atomic PDFs for pure Pt and Mn@xPt NPs. **(c)** RMC fits (red lines) to the experimental (symbols) Mn-Mn partial atomic PDFs for Mn@xPt NPs. Vertical arrows emphasize the sharpening of PDF peaks, i.e., the increase in the crystallinity of Mn core with its size. The experimental Mn-Mn partial PDFs for Mn@2Pt (blue symbols) and Mn@1Pt NPs (black symbols) are given in the inset. The PDF for Mn@2Pt NPs extends to lower-r values in comparison to that for Mn@1Pt NPs. The observation indicates that Mn-Mn atomic pair distances in Mn@xPt NPs shorten with the thickness of Pt shell. The shell shrinks accordingly. The RMC fits in (b) and (c) reflect the 3D structures shown in Fig. 2. The quality factors R_w, for the fits are in the order of 8 (± 2) %. (For interpretation of the references to colour in this figure legend, the reader is referred to the web version of this article).

aqueous solution at a scan rate of 50 mV s^{-1} under a N_2-ambient. The electrocatalytic activity for ORR was investigated by linear sweep voltammograms (LSVs) in an electrolyte of 0.1 M $HClO_4$, bubbled by O_2 for 30 min, with a scan rate of 5 mV s^{-1} and a rotation speed of 1600 rpm. In order to test the durability of the samples in an electrochemical environment, the ORR activity was measured after 5000 cycles of potential sweeps between 0.3 and 1.1 V in an O_2-saturated electrolyte.

All electrochemical measurements were performed at room temperature. The reported potentials are referenced to the reversible hydrogen electrode (RHE), and the current densities are normalized with respect to the geometric surface area of the GC electrode.

Calculations of electrochemical surface area and ORR activity

The electrochemical surface area (ECSA) of each electrocatalyst was calculated from the amount of charge of the hydrogen-desorption peak in the CV using the equation:

$$ECSA = Q_H/(m \times q_H) \quad (1)$$

where Q_H is the charge for hydrogen desorption, m is the amount of metal (Pt) in the sample, and q_H is the literature value of charge required for the adsorption of a monolayer of hydrogen on a Pt surface (210 μC cm^{-2}) [29].

For the ORR at an RDE, the Koutecky-Levich equation given below was used:

$$1/i = 1/i_k + 1/i_d \quad (2)$$

where i is the experimentally measured current, i_d is the diffusion-limiting current, and i_k is the kinetic current. For each catalyst, the kinetic current was normalized with respect to the amount of Pt and the ECSA in order to obtain the mass activity (MA, j_{mass}) and specific activity (SA, j_k) for ORR, respectively.

3. Results and discussion

3.1. Synthesis and basic characterization of Mn@Pt NPs

For brevity, the three samples of NPs studied here are referred to as Mn@xPt (x = 1, 1.5, and 2), where x refers to the number of atomic layers forming the Pt shell. As found by TEM (see Figure S1), the NPs are with a size of about 3 nm as pre-desired. Accordingly, the size of Mn core decreases as the thickness of Pt shell increases. As described above, the NPs were synthesized by one-step reactions under an ultrasound irradiation for 3 h. Although not fully understood, the formation of Mn@xPt NPs can be explained by the acoustic cavitation mechanism of sonication [30]. According to the mechanism, bubbles form, grow, and implode locally, thus generating extremely high-energy pulses, which, in turn, trigger the emergence of radicals that can reduce metal ions. Because $Mn(acac)_2$ is more volatile in comparison to $Pt(acac)_2$ [31,32], the former is preferentially evaporated into the bubbles and reacts with the radicals forming Mn° nuclei. A subsequent Pt deposition through galvanic replacement between Pt^{2+} and Mn° on the Mn nuclei results in the formation of Mn@xPt NPs [33,34].

When deposited on fine carbon powder, the NPs show a narrow size distribution and good crystallinity (see TEM and HR-TEM images in Figure S1). In house XRD patterns of the NPs are similar to the pattern of reference fcc Pt/C NPs (see Figure S2). The elemental distribution within an individual particle from each sample was probed by STEM-EDS line profiles which show clearly that the surface of Mn@xPt NPs is depleted of Mn atoms, indicative of a core-shell type structure (see Figure S3). The thickness of the Mn-depleted surface region increases systematically from ~0.3 to ~0.5 nm as x increases from 1 to 2, evidencing the increase of thickness of Pt shell from 1 to 2 Pt atomic layers. The average chemical composition of Mn@xPt NPs was measured by ICP-AES. The Mn/Pt atomic ratio in the samples was found to be 50/50, 33/67, and 26/74 for x = 1, 1.5, and 2, respectively, (see Table S1). Values are consistent with the Mn@xPt core-shell structures to be detailed below, which are, in turn consistent with HR-TEM and STEM-EDS images showing NPs with an average size of 3 nm and shell thicknesses of 1–2 atomic layers.

3.2. Synchrotron X-ray experiments and 3D structure modeling

In order to reveal the atomic-scale structure of Mn@xPt NPs in better detail, we carried out resonant HE-XRD experiments at the K edge of Pt atoms (78.395 keV). The experiments involved measuring two diffraction patterns close to but below the adsorption edge of Pt (Figure S4), taking the difference between the two patterns, and Fourier transforming it into the so-called Pt-differential PDF. The Mn-Mn partial and total PDFs for Mn@xPt NPs were also obtained. Details are

given in the SM and Refs. [35,36]. Exemplary HE-XRD patterns for reference Pt and Mn@xPt NPs are shown in Figure S5. The respective total and Mn-Mn partial PDFs are shown in Figs. 1(a,b) and 1(c), respectively. Note that, as shown in Figure S6, the total PDFs are different from those for Fe@Pt NPs studied previously [27]. Also, note that unlike local-probe techniques such as extended x-ray absorption fine structure spectroscopy, element-specific atomic PDFs obtained by resonant HE-XRD can reveal interatomic correlations extending up to distances equal to the diameter (size) of the studied NPs. As demonstrated below, this greatly facilitates constructing realistic 3D models for Mn@xPt NPs.

Total PDFs for pure Pt and Mn@xPt NPs were fit with models constrained to the fcc-type crystal structure of bulk Pt. Computational details are given in the SI. Results of the computations are shown in Fig. 1(a). As can be seen in the Figure, the experimental total PDF for pure Pt NPs is reproduced reasonably well by the model. The experimental total PDFs for Mn@xPt NPs, however, are not quite well reproduced by it. Furthermore, the values for the refined fcc-lattice parameter for the NPs appear scattered. The observations indicate that, though exhibiting HE-XRD patterns similar to that of pure Pt NPs (see Figures S2 and S5), Mn@xPt NPs are unlikely to be stacks of close packed atomic layers known to occur with bulk fcc metals and alloys.

To obtain a better insight into the atomic arrangement in Mn@Pt NPs, we constructed full-scale models for the NPs using Molecular Dynamics (MD) and reverse Monte Carlo (RMC) computations. To be as realistic as possible, the models reflected the average size (~3 nm), shape (polyhedra with round edges; see Figure S1), morphology (core-shell) and overall chemical composition of the modeled NPs. A model for pure Pt NPs was also constructed. Initially, the model atomic configurations were relaxed in terms of energy, i.e. stabilized at atomic level, by MD. The MD-relaxed models were refined against the respective total and Mn-Mn partial PDFs by RMC. The refinement was necessary because metallic NPs can exhibit specific atomic-level features, such as considerable surface structural relaxation, which may not be captured well by MD alone, i.e. without experimental input [37]. The thermal (Debye − Waller type) and static displacements, i.e. relaxation, of atoms in the refined models were treated separately. In addidion, the energy of RMC refined models was minimized further using pair-wise potentials taken from literature sources. Details of the MD and RMC computations are given in the SI. The refined models are shown in Fig. 2. The distribution of bond angles in the Mn core and Pt shell of the models are shown in Figure S7(a) and S7(b), respectively. As can be seen in the Figures, Pt atoms arrange in an fcc-type manner while Mn atoms form more or less disordered bcc-type configurations. Data in Figure S7(a) also indicate that the degree of disorder in Mn cores diminishes with their size, i.e. is inversely proportional to the thickness of Pt shell (follow the strengthening of the sharp features in the distributions marked with vertical solid arrows). The increasing crystallinity of larger Mn cores is also seen as a sharpening of the peaks in the respective Mn-Mn partial PDFs shown in Fig. 1(c) (follow the vertical dotted arrows). Data in Figure S7(b) indicate that the opposite is true for Pt shell, i.e. it becomes more disordered locally with its size (follow the non-negligible broadening of the distributions marked with a horizontal dotted arrow). Altogether, the models appear fully consistent with the experimental i) HR-TEM data in terms of size and shape, ii) STEM-EDS profiles in terms of a mutual distribution of Mn and Pt atoms, iii) ICP-AES data in terms of overall chemical composition and iv) reproduce the experimental total and partial Mn-Mn PDFs data in very good detail (see Figs. 1a and 1b). As such, within the limits of experimental accuracy, the models can be considered as the most likely, ensemble-averaged 3D atomic structures of pure Pt and Mn@xPt NPs studied here, and so are fit for their purpose. That is, the structures can be used as a rational basis for evaluating the unusual catalytic properties of the NPs [27,37], which are discussed further below.

3.3. Electrochemical characterization of Mn@xPt NPs

The electrochemical properties of carbon supported Mn@xPt NPs as catalysts for ORR were studied by CV and LSV. CV curves for Mn@xPt and reference Pt/C NPs are shown in Fig. 3(a). The curves show two pairs of redox peaks, which are characteristic to Pt-based catalysts. The first pair is associated with hydrogen adsorption and desorption (0.0 - 0.3 V), and the second pair oxide formation and decomposition (0.6 - 0.9 V). Also, the curves appear stable for up to 100 cycles, indicating that Mn atoms in the core of Mn@xPt NPs are well protected from direct (electro)chemical reactions.

ECSAs of the NPs were estimated by integrating the peaks at 0.0 - 0.3 V region in the anodic sweep for the hydrogen desorption from the Pt surface (H_{UPD}), using the reference value of 210 μC cm^{-2} for an annealed Pt surface [29]. The normalized ECSAs per unit Pt mass are in the order of Mn@2Pt > Mn@1.5 Pt > Mn@Pt > Pt (see Fig. 3(d)). The fact that Mn@xPt NPs have larger ECSAs than corresponding Pt NPs is understandable because Pt species in the former are 'diluted' in comparison to the latter. Surprisingly, however, within the series of Mn@xPt NPs, ECSA increases as x increases. This trend is counter-intuitive because the x = 1 composition is the most Pt-dilute and, hence, is expected to have the largest ECSA. The slight decrease of the average particle size from 2.9 to 2.7 and then to 2.6 nm with x

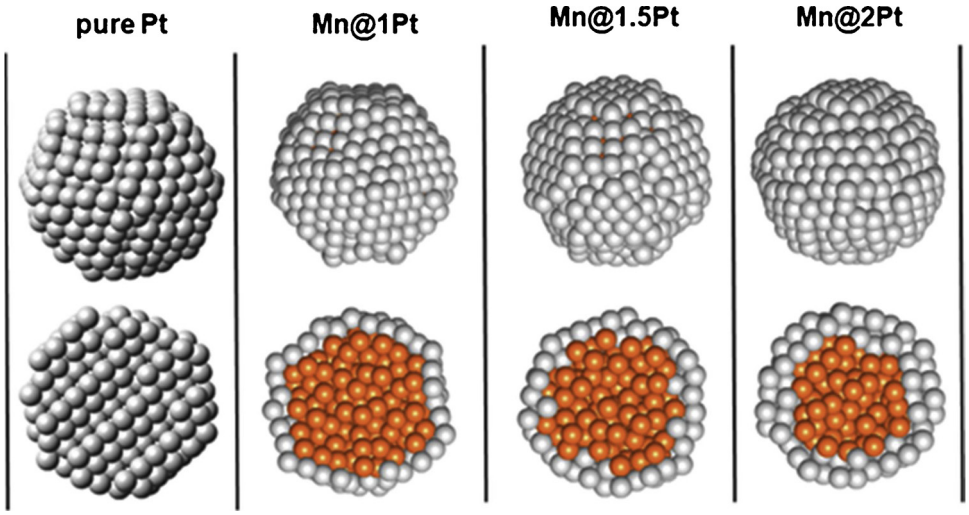

Fig. 2. (**first row**) 3D model structures for pure fcc Pt and bcc-like Mn@fcc-like Pt NPs determined as described in the text. (**second row**) Cross sections of the respective structures. Pt atoms are in gray and Mn atoms are in light brown.

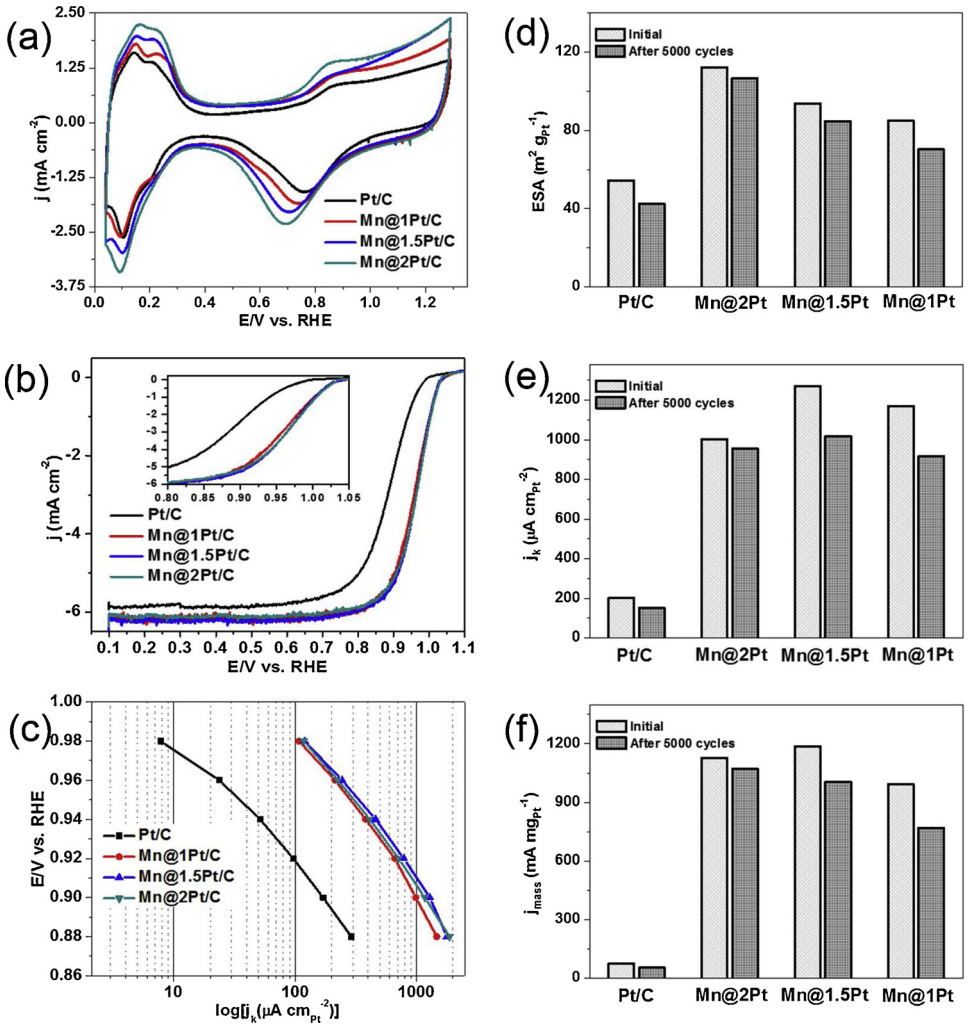

Fig. 3. (**left**) Electrochemical data for Mn@1Pt, Mn@1.5 Pt, and Mn@2Pt NPs deposited on carbon support: (a) Cyclic Voltammograms (Inset is CV of Pt/C), (b) Linear Sweep Voltammograms (Inset is a magnified view for the potential range of 0.80–1.05 V), and (c) Tafel plots. (**right**) Comparison of the electrochemical data of Mn@1Pt, Mn@1.5 Pt, and Mn@2Pt NPs deposited on carbon support and a reference Pt/C. Data for fresh and cycled (5,000 potential cycles) are given. (d) Electrochemically active surface areas and (e) Specific activity and (f) Mass activity taken at 0.9 V.

increasing from 1 to 1.5 and then to 2, respectively, may contribute to this trend. However, it cannot account for the trend completely because the fraction of Pt species unused for H_{UPD} increases very fast when x increases. DFT calculations of the binding energy of H atoms to a surface comprising one or two (111) Pt layers positioned on top of a Mn layer (Table S4) show that the two-layer surface binds H stronger than the one-layer one. The result indicates that the ECSA of Mn@1Pt NPs may be underestimated in comparison to Mn@xPt NPs with x = 1.5 or 2. The largely different facets of Mn@xPt NPs, indicated by the respective 3D models shown in Fig. 2, may also affect the strength with which H atoms bind to their surfaces. In particular, the peaks at 0.12 V and 0.24 V in the H-desorption curve are attributed to desorption of H from Pt(110) and Pt (100) facets, respectively. The H desorption from Pt(111) is reported to give a peak between these two. The CVs of pure Pt and Mn@1Pt NPs show prominent peaks related to H desorption from Pt(100) and Pt(110) facets. As the thickness of the Pt shell increases, the two peaks smear out and nearly overlap completely. Such a trend is observed with pure Pt NPs whose size decreases and, hence, surface becomes less regular [38]. The CVs also show the reduction peaks of surface oxides on the NPs at ~0.7 V. All of the Mn@xPt samples show lower reduction potentials than Pt/C. Typically, a lower peak potential is considered as a sign of increased stability of surface oxides [39]. Therefore, per the CV data, Mn cores seem to increase the affinity of Pt shells to oxygen atoms. Furthermore, contrary to common knowledge, the stability of oxides on the surface of Mn@xPt NPs apparently increases with the Pt content increases. These observations will be discussed later.

LSV curves obtained in an oxygen-saturated 0.1 M $HClO_4$ solution are summarized in Fig. 3b. As can be seen in the Figure, the onset potential of Mn@xPt NPs (~1.05 V vs. RHE) is higher than that of reference Pt/C (0.99 V vs. RHE) by ~60 mV. The steeper slopes of Mn@xPt in the 0.8–1.0 V region of the LSV curves and the Tafel plots shown in Fig. 3(c) indicate that the kinetics of ORR is significantly faster with Mn@xPt NPs in comparison to reference Pt/C. The specific and mass activities of reference Pt and Mn@xPt NPs, normalized with respect to ECSAs and the amounts of used Pt, are shown in Figs. 3(e) and (f), respectively. Data in the Figures show that Mn@xPt NPs outperform pure Pt NPs as ORR catalysts by a factor of 5–6.5 for SA and by 14–16 for MA. Among the Mn@xPt catalysts, Mn@1.5 Pt shows the highest SA and MA. The SA of Mn@1Pt NPs is higher than that of Mn@2Pt NPs whereas the order is reversed when MA of the NPs is compared. Here is to be noted that among the series of TM@Pt NPs synthesized by the sonochemical reaction method, where TM is Mn, Fe, Co, and Ni [33,34,40,41], the Mn@xPt NPs system studied here stands out not only for its higher electrocatalytic activity but also for the trends it shows. These peculiarities of Mn@xPt NPs will be discussed later.

Catalytic stability is an important factor to consider when developing advanced ORR catalysts for fuel cells related applications. LSV

curves for Mn@xPt NPs undergone 5000 cycles in the potential range of 0.3–1.1 V in O_2-saturated 0.1 M $HClO_4$ solution at room temperature and for the respective not-cycled NPs are shown in Figure S8. The calculated values of ECSAs, SA, and MA from the CVs and LSVs before and after the potential cycling are summarized in Table S2. While cycled reference Pt/C suffers 27.1 % loss in activity, the ORR activity of cycled Mn@xPt NPs drops by only 5–22%. Here, the ORR stability of Mn@2Pt NPs (4.9 % loss after 5,000 cycles) is particularly remarkable. The TEM image of this sample shows that the NPs are almost intact after the cycling (see Figure S9).

3.4. Structure-ORR activity relationship for Mn@xPt NPs

The electrochemistry data show that the core in Mn@xPt NPs greatly enhances the catalytic activity of Pt shell for ORR. Studies have shown that the reaction proceeds via a number of steps including, among others, the cleavage of strong O═O bond in molecular oxygen adsorbed on the catalyst surface, and removal of reaction intermediates such as *OH and *OOH groups leading to the formation of water. Here "*" denotes an active surface site capable of binding ORR reactants and reaction intermediates. The present understanding is that an efficient ORR catalyst would bind oxygen molecules with ample strength to allow the cleavage of O═O bonds and formation of *O but weakly enough to liberate the reaction intermediates and products when the reaction is complete. In addition, it is considered that the binding energy of *OH, *OOH, O_2 and atomic oxygen *O are strongly correlated and so the binding energy of the latter can serve as an indicator for catalytic activity for the ORR [42–44]. In addition, it is considered that a moderate decrease in the binding energy of atomic oxygen to Pt surfaces would increase their activity for ORR [12]

DFT calculations on the adsorption properties of atomic oxygen on model slabs composed of 1 and 2 ML Pt formed on Mn slabs were performed. Jennings et al. showed that the adsorption properties of oxygen species on the slab model show the same tendency as those on the terraces of NP models [45]. Therefore, the slab model calculations will be sufficient to account for the electronic effects of Pt-Mn interaction in explaining the observed electrocatalytic trends in Fig. 3e and 3f. The results show that both atomic oxygen and hydrogen bind more strongly to the surface of 2 ML Pt than 1 ML Pt (see Table S4 and S5). In the ORR process, an oxygen molecule is decomposed to two oxygen atoms, and they form water molecules with hydrogen atoms. If oxygen atoms are adsorbed too strongly, excessively large adsorption energy of oxygen atoms hinders the ORR reaction [46,47]. Therefore, the DFT results suggest that Mn@1Pt will show higher SA than Mn@2Pt, which agrees with the observation. However, the DFT results cannot explain some of the observed data such as the opposite trend of MA and the highest SA and MA of Mn@1.5 Pt. Hence, we considered other possible explanations using experimental and not assumed structural characteristics of Mn@xPt NPs.

Generally, the reactivity of Pt surfaces toward oxygen and oxygenated species (*OH/*OOH) is largely determined by the width, w_d, and energy position, ε_d, of the *d*-band of surface Pt atoms, degree of hybridization of their valence 6(*s,p*) and 5d electrons, and the resulting electron density of *d*-states (*d*-DOS) near the Fermi energy. According to electronic structure theory of metals, w_d, ε_d and *d*-DOS depend strongly on the local coordination of metal atoms, in particular on their first coordination number and radii. Therefore, we used the so-called effective surface coordination numbers (CN_{eff}) and distances between surface Pt atoms in pure Pt and Mn@xPt NPs to directly assess their catalytic activity for ORR. The CN_{eff} and Pt-Pt distances computed from the positions of atoms in the respective 3D models are shown in Fig. 4(a–d) and Fig. 5(a–d), respectively. Details of the computations are given in the SI. Here is to be noted that the approach of using CN_{eff} instead of the traditional counting of near neighbors is similar to the embedded-atom method, where the valence electron density at an atomic site is approximated by a superposition of the valence electron density of the nearby atoms which, in turn, is a superposition of the valence electron density of the first neighbors for those atoms [48].

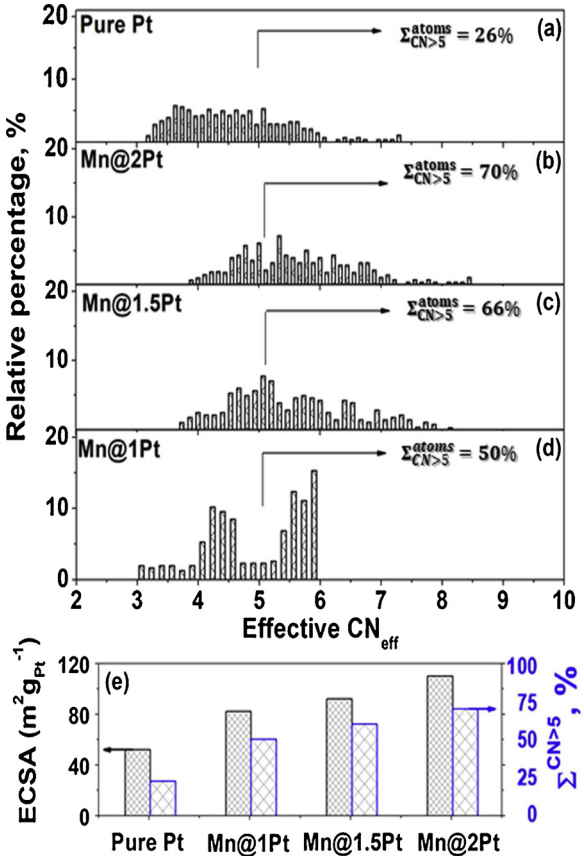

Fig. 4. Effective coordination numbers for surface Pt atoms in (a) pure Pt NPs, (b) Mn@2Pt NPs, (c) Mn@1.5 Pt NPs and (d) Mn@1Pt NPs. The fraction of surface Pt atoms with $CN_{eff} > 5$ is given for each data set. Note that the maximum CN_{eff} for atoms occupying a close packed Pt monolayer is 6. That number is 9 for atoms at the $(111)_{fcc}$ facet of bulk Pt (6 neighbors from the same surface layer and 3 from the layer beneath it). (e) Comparison between experimental ECSA values (bars outlined in gray) and percentage of surface Pt atoms with $CN_{eff} > 5$ (bars outlined in blue). (For interpretation of the references to colour in this figure legend, the reader is referred to the web version of this article).

As can be seen in Fig. 4, the relative percentage of top surface atoms in pure Pt, Mn@1Pt, Mn@1.5 Pt and Mn@2Pt NPs with $CN_{eff} > 5$ is 26, 50, 66, and 70 %, respectively. The percentages make sense at least because the fraction of atoms on the densely packed $(111)_{fcc}$ facets of Pt NPs with a cubooctahedral shape and size of 2 − 3 nm is known to be in the range of 20 % to 30 % (e.g. see Fig. 5 in Ref. [11]]. According to the *d*-band center theory, bond order conservation arguments and experimental observations, higher coordinated Pt atoms on flat surfaces, such as $(111)_{fcc}$-type terraces, would show enhanced catalytic activity for ORR in comparison to lower coordinated Pt atoms [12,48,49]. The larger number of surface Pt atoms with $C_{Neff} > 5$ in Mn@xPt NPs in comparison to pure Pt NPs, and the relative increase of that number with the thickness of Pt shell correlate well with the observed trend of ECSA for the NPs (compare data in Figs. 3d and 4e). Also, the near bimodal distribution of CN_{eff} in Mn@1Pt NPs on one hand (i.e. well-defined facets), and the much broader distribution of CN_{eff} in Mn@1.5 Pt and Mn@2Pt NPs on the other (i.e. uneven facets), correlate well with the observed trend in the shape of the H-desorption curves for the NPs in the 0.1 - 0.3 V region (see data in Fig. 3a).

Comparison between the data in Figs. 4 and 5 shows that the observed increase in CN_{eff} may be associated with the significant increase in the compressive strain, i.e., shortening of Pt-Pt bonding distances in Mn@xPt NPs. The shortening would increase the overlap of 5*d* orbitals

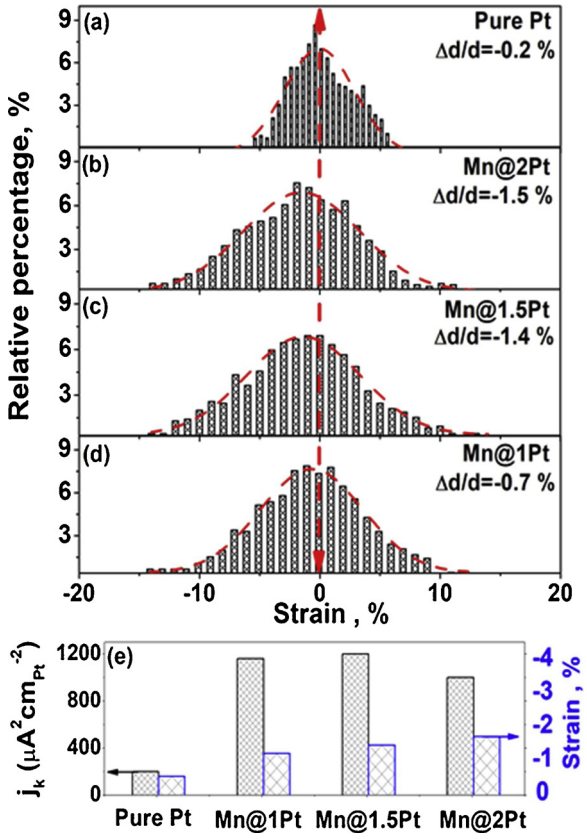

Fig. 5. Distribution of Pt-Pt bonding distances/surface strain in (a) pure Pt NPs (b) Mn@2Pt NPs, (c) Mn@1.5 Pt NPs and (d) Mn@1Pt NPs. Values are normalized (in %) against the bulk Pt-Pt bonding distance, ***d***, of 2.775 Å. The average value of surface strain $\Delta d/d$ is given for each data set. (e) Comparison between experimental values for specific ORR activity (bars outlined in gray) and average surface strain (bars outlined in blue). An increased compressive surface strain is seen to correspond to an increased specific activity for ORR. (For interpretation of the references to colour in this figure legend, the reader is referred to the web version of this article).

and so the energy of 5*d* electrons of nearby surface Pt atoms in Mn@xPt in comparison to those in pure Pt. The significantly decreased CN_{eff} in Mn@xPt NPs in comparison to the bulk value of 12 would diminish the degree of delocalization of the valence 5*d* electrons of the surface Pt atoms in the NPs and so narrow the surface w_d. This would increase the energy of 5*d* electrons of surface Pt atoms further due to increased Coulomb repulsion. Then, it may be conjectured that some 5*d* electrons of surface Pt atoms in Mn@xPt NPs would be promoted to higher energy 6*sp* bands through 5*d* → 6*sp* charge redistribution (*sp-d* hybridization) leading to a net decrease of the *d*-DOS of the atoms. A somewhat decreased occupation of surface Pt 5*d*-band, i.e. an increased number of the so-called 5*d*-vacancies, would lead to an increase in the core-level binding energy for Pt atoms in Mn@xPt NPs, as documented by XPS (see data in Figure S10 and Table S3). Furthermore, it would increase the oxophilicity of Mn@xPt NPs, eventually leading to the formation of Pt-Ox oxide-like surface sites. The magnitude of the latter though would depend on the particular number of 5d vacancies, percentage and type of active Pt surface sites and so may be expected to vary with the thickness of Pt shell as observed by the electrochemical experiments (Fig. 3a) and predicted by DFT calculations (see Tables S5) done here. As discussed in Refs. [7,8,17,50], a moderately increased absorption energy of oxygenated species may indeed have a net positive effect on the ORR activity of Pt surfaces. That is because it may weaken: i) O═O bonds and so facilitate the dissociative absorption of oxygen molecules, thereby generating more *O species available to interact with other nearby species and ii) the adsorption energy of reaction intermediates such as *OH, thereby reducing their 'poisoning' effect/negative impact on the ORR kinetics. The latter may be rationalized in terms of increased lateral repulsive interactions between nearby *OH species, forcing them occupy less favored surface sites. Ultimately, the kinetics of ORR over the surface of Mn@xPt NPs would improve in comparison to pure Pt NPs.

An inspection of data in Figs. 4(e) indicates that, due to the 2- to 3-fold increase in the percentage of surface sites with $CN_{eff} > 5$, the improvement would be at least by a factor of two or three. When the differences in the percentage of Pt species in pure Pt NPs and Mn@xPt NPs are taken into account, the improvement factor would be even higher, as indeed observed here.

It is important to clarify the contribution of Mn core in Mn@xPt NPs to their superb catalytic activity for ORR. Among all transition metals, Mn has the most complex atomic-scale structure. The room temperature phase of Mn (α-Mn), has a body-centered cubic cell occupied by 58 atoms with CNs varying from 12 to 16. The Mn-Mn bonding distances vary from 2.24 Å to 2.91 Å. Beta Mn (β-Mn), appearing in the temperature range from 1000 K to 1368 K, has a simple cubic unit cell populated with 20 Mn atoms, each having a CN of 12. Mn-Mn bonding distances vary from 2.36 Å to 2.67 Å. The fcc γ-phase of Mn (γ-Mn) is stable in the temperature range from 1368 K to 1406 K. At higher temperatures up to the melting point of 1517 K, the bcc *δ*-phase of Mn (-Mn) appears. The average atomic volume of Mn atoms in -Mn, -Mn, -Mn and *δ*-Mn) appears. The average atomic volume of Mn atoms in α-Mn, β-Mn, γ-Mn and *δ*-Mn, also known as the Wigner-Seitz volume of Mn, is approximately 12.1, 12.5, 14.6 and 14.9 Å^3, respectively. That is, due to the strong rms vibrations of the constituent atoms at high temperatures, *δ*-Mn appears both less ordered and less densely packed at atomic level in comparison to the other phases of Mn. In addition, the bulk modulus, B, of *δ*-Mn is about 12 % smaller than that of α-Mn (~120 GPa), which, in turn, is smaller than those of bcc Fe (170 GPa), bcc Cr (160 GPa), fcc Co (210 GPa) and fcc Ni (200 GPa) [51–53]. Thus, bcc *δ*-Mn also appears rather soft mechanically as compared to the other phases of Mn. Experimental Mn-Mn partial PDFs for Mn@xPt NPs and PDFs computed from the four crystalline modifications of bulk Mn are compared in Figure S11. Data in the Figure show that the arrangement of nearby Mn atoms in Mn@xPt NPs resembles that in *δ*-Mn and, furthermore, does not change its type with the core's size. Furthermore, analysis of both the distribution of bond angles in Mn cores (Figure S7(a)) and the evolution of peaks in the experimental Mn-Mn partial PDFs (follow the vertical dotted arrows in Fig. 1c) indicate that, as their size increases, the cores gradually become more crystalline, i.e. more ordered, in nature. On the other hand, as the distribution of Pt-Pt-Pt bond angles in Figure S7(b) shows, the Pt shells of Mn@Pt NPs are fcc-like ordered and become more distorted (follow the horizontal red arrow) with their thickness. Altogether, it appears that, as synthesized, Mn cores of Mn@xPt NPs adopt the structure type of the less ordered, low density and soft *δ*-Mn form of bulk Mn. When kept relatively small in size (~150 atoms) and covered with two layers of densely packed fcc Pt (~450 atoms), which is the case of Mn@2Pt NPs, the cores both remain disordered at atomic level and densify. In turn, Pt layers become uneven and considerably compressed (~1.5 %; see Fig. 5b), i.e. exhibiting a broad distribution of surface sites involving closely packed Pt atoms (Fig. 4b). When let to double in size (~300 atoms) and then covered with a monolayer of Pt (~300 atoms) alone, the cores appear somewhat both more crystalline (i.e. ordered) in nature and resilient to external pressure. Hence, the cores keep their atomic packing density, or at least do not densify as much as observed with Mn@2Pt NPs (compare the shape and position of the first peak in Mn-Mn PDFs shown the inset in Fig. 1c). In turn, the Pt monolayer appears moderately compressed (~0.7 %; see Fig. 5d) and relatively uniform, i.e. exhibiting a relatively narrow distribution of surface sites involving closely packed Pt atoms (see data in Fig. 4d). The structural characteristics of Mn@1.5 Pt NPs range between those of Mn@1Pt and Mn@2Pt NPs.

We argue that, due to its intrinsically open structure and softness,

Mn endows Pt shell in Mn@Pt NPs with superb catalytic activity for ORR. In particular, depending on both their size and thickness of Pt shell that covers them, Mn cores appear with a different degree of structural disorder and atomic packing density. In turn, depending on both the size of pre-made Mn cores and its thickness, the Pt shell deposited on the cores appears compressed and uneven to a different extent. Furthermore, within a particular range of Mn to Pt ratios in the NPs, the thickness of Pt shell, its compression and disorder can evolve in inverse proportions. That is, the surface atomic structure of Mn@xPt NPs, in particular the coordination environment of surface Pt atoms and related atomic-level stresses, may be more diverse in comparison to TM@Pt NPs studied so far, where TM cores are inherently dense packed at atomic level (e.g. fcc Ni, Cu and fcc/hcp Co) and/or mechanically rigid (e.g. bcc Fe). Therefore, nearby surface Pt sites in the former are likely to exhibit significantly different ORR activity in comparison to those in the latter, at least because 5*d*-orbitals at the sites would overlap and/or orient in 3D space differently. The effect may be such that the scaling relationship between the binding energy of oxygenated species changes in a way promoting the kinetic of ORR over Mn@Pt NPs beyond the level observed with TM@Pt NPs. In particular, the binding energy of O_2 is increased and so the breaking of O═O bond is facilitated without correspondingly increasing the binding strength of OH and OOH species [43,44,48]. All this puts the inherently structurally diverse Mn on the forefront of the effort to develop more efficient and affordable core-shell catalyst for ORR and other reaction driving energy related applications.

4. Conclusions

A large fraction of mankind's energy consumption is used for transportation. Fuel cell technologies offer big promise for replacing the huge use of fossil fuels with clean renewable resources at a fraction of the cost. Strategies for improving the performance of Pt-based catalysts for fuel cell applications are based on the understanding that pure Pt binds ORR reaction intermediates too strongly for the reaction to proceed at a high rate. Moderate compression weakens the reactivity of Pt, rendering 3*d*-metal atoms suitable substitutes for the larger size 5*d* Pt atoms. Catalysts composed of a Mn core and thin Pt shell are particularly promising because i) Mn atoms are prone to change their packing density under external stimuli and ii) Pt atoms are prone to pack densely in an fcc manner. This makes it possible to tune the core and shell components of Mn@Pt NPs relative to one another, endowing the resulting particles with superb activity for ORR.

CRediT authorship contribution statement

Md. Abdul Matin: Conceptualization, Methodology, Visualization. **Junsu Lee:** Formal analysis. **Gwan Woo Kim:** Formal analysis. **Hyun-Uk Park:** Methodology, Validation. **Byeong Jun Cha:** Investigation. **Sarvjit Shastri:** Investigation. **Gunn Kim:** Formal analysis. **Young-Dok Kim:** Investigation. **Young-Uk Kwon:** Supervision, Resources, Writing - review & editing. **Valeri Petkov:** Writing - original draft, Investigation, Formal analysis.

Declaration of Competing Interest

The authors declare that they have no known competing financial interests or personal relationships that could have appeared to influence the work reported in this paper.

Acknowledgements

This work was supported by the National Research Foundation of Korea under grant NRF-2016R1A2B4014012, and by Ministry of Trade, Industry, and Energy (MOTIE), Korea, under the "Commercializing fuel cell electric vehicle component industry and R&D Support Program"(P0000273) supervised by the Korea Institute for Advancement of Technology (KIAT). It was also supported by DOE-BES Grant DE-SC0006877 and used resources of the Advanced Photon Source at the Argonne National Laboratory provided by the DOE Office of Science under Contract No. DE-AC02-06CH11357.

Appendix A. Supplementary data

Supplementary material related to this article can be found, in the online version, at doi:https://doi.org/10.1016/j.apcatb.2020.118727.

References

[1] T. Hao, C. Zhang, P. Su, Z. Shen, H. Liu, G. Wang, S. Liu, J. Liu, Metal-organic-Framework-derived formation of Co–N-doped carbon materials for efficient oxygen reduction reaction, Int. J. Energ. Mater. Chem. Propuls. 40 (2020) 137–143.
[2] I.E.L. Stephens, A.S. Bondarenko, U. Grønbjerg, J. Rossmeisl, I. Chorkendorff, Understanding the electrocatalysis of oxygen reduction on platinum and its alloys, Energy Environ. Sci. 5 (2012) 6744–6762.
[3] I.E.L. Stephens, J. Rossmeisl, I. Chorkendorff, Toward sustainable fuel cell, Science 354 (2016) 1378–1379.
[4] A.H. Gasteiger, S.S. Kocha, B. Sopalli, F.T. Wagner, Activity benchmarks and requirements for Pt, Pt-Alloy, and Non-Pt oxygen reduction catalysts for PEMFCs, Appl. Catal. B: Environ. 56 (2005) 9–35.
[5] B.C.H. Steele, A. Heinzel, Materials for fuel-cell technologies, Nature 414 (2001) 345–352.
[6] H. Lv, D. Li, D. Strmcnik, A.P. Paulikas, N.M. Markovic, V.R. Stamenkovic, Recent advances in the design of tailored nanomaterials for efficient oxygen reduction reaction, Nano Energy 29 (2016) 149–165.
[7] T. Toda, H. Igarashi, H. Uchida, M. Watanabe, Enhancement of the electroreduction of oxygen on Pt alloys with Fe, Ni, and Co, J. Electrochem. Soc. 146 (1999) 3750–3756.
[8] S. Mukerjee, S. Srinivasan, M.P. Soriaga, J. McBreen, Role of Structural and Electronic Properties of Pt and Pt Alloys on Electrocatalysis of Oxygen Reduction. An In Situ XANES and EXAFS Investigation, J. Electrochem. Soc. 142 (1995) 1409–1422.
[9] P. Strasser, S. Koh, T. Anniyev, J. Greeley, K. More, C. Yu, Z. Liu, S. Kaya, D. Nordlund, H. Ogasawara, M.F. Toney, A. Nilsson, Lattice-strain control of the activity in dealloyed core-shell fuel cell catalysts, Nat. Chem. 2 (2010) 454–460.
[10] A. Sarker, A. Manthiram, Synthesis of Pt@Cu core − Shell nanoparticles by galvanic displacement of Cu by Pt^{4+} ions and their application as electrocatalysts for oxygen reduction reaction in fuel cells, J. Phys. Chem. C 114 (2010) 4725–4732.
[11] K. Sasaki, A. Kuttiyiel, D. Su, R.R. Adzic, Platinum Monolayer on IrFe Core–Shell Nanoparticle Electrocatalysts for the Oxygen Reduction Reaction, Electrocatalyst 2 (2011) 134–140.
[12] J.X. Wang, H. Inada, L. Wu, Y. Zhu, Y. Choi, P. Liu, W.-P. Zhou, R.R. Adzic, Oxygen reduction on well-defined core − Shell nanocatalysts: particle size, facet, and Pt shell thickness effects, J. Am. Soc. Brew. Chem. 131 (2009) 17298–17302.
[13] X. Huang, Z. Zhao, L. Cao, Y. Chen, E. Zhu, Z. Lin, M. Li, A. Yan, A. Zettl, Y.M. Wang, X. Duan, T. Mueller, Y. Huang, High-performance transition metal–Doped Pt_3Ni octahedra for oxygen reduction reaction, Science 348 (2015) 1230–1234.
[14] C. Cui, L. Gan, H.-H. Li, S.-H. Yu, M. Heggen, P. Strasser, Octahedral PtNi nanoparticle catalysts: exceptional oxygen reduction activity by tuning the alloy particle surface composition, Nano Lett. 12 (2012) 5885–5889.
[15] S.-I. Choi, S. Xie, M. Shao, J.H. Odell, N. Lu, H.-C. Peng, L. Protsailo, S. Guerrero, J. Park, X. Xia, J. Wang, M.J. Kim, Y. Xia, Synthesis and characterization of 9 nm Pt–Ni octahedra with a record high activity of 3.3 A/mg_{Pt} for the oxygen reduction reaction, Nano Lett. 13 (2013) 3420–3425.
[16] P. Strasser, S. Kühl, Dealloyed Pt-Based core-shell oxygen reduction electrocatalysts, Nano Energy 29 (2016) 166–177.
[17] V. Stamenkovic, T.J. Schmidt, P.N. Ross, N.M. Markovic, Surface composition effects in Electrocatalysis: kinetics of oxygen reduction on well-defined Pt_3Ni and Pt_3Co alloy surfaces, J. Phys. Chem. B 106 (2002) 11970–11979.
[18] J.L. Reyes-Rodriguez, F. Godinez-Salomon, M.A. Leyva, O. Soloza-Feria, RRDE study on Co@Pt/C-Core shell nanocatalysts for the oxygen reduction reaction, Int. J. Hydrogen Energy 38 (2013) 12634–12639.
[19] X. Zhang, H. Wang, J. Key, V. Linkov, S. Ji, X. Wang, Z. Lei, R. Wang, Strain effect of core-shell Co@Pt/C nanoparticle catalyst with enhanced electrocatalytic activity for methanol oxidation, J. Electrochem. Soc. 159 (2012) B270–B276.
[20] K.A. Kuttiyiel, K. Sasaki, D. Su, P. Liu, R.R. Adzic, Nitride stabilized PtNi core–Shell nanocatalyst for high oxygen reduction activity, Nano Lett. 12 (2012) 6266–6271.
[21] G. Wang, H. Wu, D. Wexler, H. Liu, O. Savadogo, Ni@Pt Core-Shell Nanoparticles with Enhanced Catalytic Activity for Oxygen Reduction Reaction, J. Alloys. Compd. 503 (2010) L1–L4.
[22] L. Bu, N. Zhang, S. Guo, X. Zhang, J. Li, J. Yao, T. Wu, G. Lu, J.-Y. Ma, D. Su, X. Huang, Biaxially strained PtPb/Pt Core/Shell nanoplate boosts oxygen reduction catalysis, Science 354 (2016) 1410–1414.
[23] Y. Kang, C.B. Murray, Synthesis and electrocatalytic properties of cubic Mn − Pt nanocrystals (Nanocubes), J. Am. Soc. Brew. Chem. 132 (2010) 7568–7569.
[24] B. Lim, T. Yu, Y. Xia, Shaping a bright future for platinum-based alloy electrocatalysts, Angew. Chem. Int. Ed 49 (2010) 9819–9820.

[25] V.R. Stamenkovic, B.S. Mun, M. Zrenz, K.J.J. Mayrhofer, C.A. Lucas, G. Wang, P.N. Ross, N.M. Markovic, Trends in Electrocatalysis on extended and nanoscale Pt-Bimetallic alloy surfaces, Nat. Mater. 6 (2007) 241–247.
[26] P. Vanýsek, Electrochemical series, in: W.M. Haynes (Ed.), Handbook of Chemistry and Physics, 93rd edition, Chemical Rubber Company, 2012, pp. 5–80.
[27] V. Petkov, B. Prasai, S. Shastri, H.-U. Park, Y.-U. Kwon, V. Skumryev, Ensemble averaged structure–function relationship for nanocrystals: effective super-paramagnetic Fe clusters with catalytically active Pt skin, Nanoscale 9 (2017) 15505–15514.
[28] J.P. Perdew, K. Burke, M. Ernzerhof, Generalized gradient approximation made simple, Phys. Rev. Lett. 77 (1996) 3865–3868.
[29] F.C. Nart, W. Vielstich, W. Vielstich, A. Lamn, H. Gasteiger (Eds.), Handbook of Fuel Cells: Fundamentals Technology and Applications, vol. 2, John Wiley & Sons Ltd., Chichester, 2003, pp. 302–315.
[30] K.S. Suslick, Sonochemistry, Science 247 (1990) 1439–1445.
[31] E.W. Berg, J.T. Truemper, Vapor pressure-temperature data for various metal β-diketone chelates, Anal. Chem. Acta 32 (1965) 245–252.
[32] N.B. Morozova, G.I. Zharkova, P.P. Semyannikov, S.V. Sysoev, I.K. Igumenov, N.E. Fedotova, N.V. Gelfond, Vapor pressure of precursors for CVD on the base of platinum group metals, J. Phys. IV France 11 (2001) 609–616.
[33] J.-H. Jang, E. Lee, J. Park, G. Kim, S. Hong, Y.-U. Kwon, Rational syntheses of core-shell Fe_x@Pt nanoparticles for the study of electrocatalytic oxygen reduction reaction, Sci. Rep. 3 (2013) 2872.
[34] J.-H. Jang, J. Kim, Y.-H. Lee, I.Y. Kim, M.-H. Park, C.-W. Yang, S.-J. Hwang, Y.-U. Kwon, One-pot synthesis of core-shell-Like Pt_3Co nanoparticle electrocatalyst with Pt-Enriched surface for oxygen reduction reaction in fuel cells, Energy Environ. Sci. 4 (2011) 4947–4953.
[35] V. Petkov, S. Shastri, Element-specific structure of materials with intrinsic disorder by high-energy resonant X-Ray diffraction and differential atomic pair-distribution functions: a study of PtPd nanosized catalysts, Phys. Rev. B 81 (2010) 165428.
[36] Y. Waseda, Anomalous X-Ray Scattering for Materials Characterization: Atomic-Scale Structure Determination, Springer, Berlin, 2002.
[37] V. Petkov, B. Prasai, Y. Ren, S. Shan, J. Luo, P. Joseph, C.-J. Zhong, Solving the nanostructure problem: exemplified on metallic alloy nanoparticles, Nanoscale 6 (2014) 10048–10061.
[38] C.M. Zalitis, A.R. Kucernak, J. Sharman, E. Wright, Design principles for platinum nanoparticles catalyzing electrochemical hydrogen evolution and oxidation reactions: edges are much more active than facets, J. Mater. Chem. A Mater. Energy Sustain. 5 (2017) 23328–23338.
[39] S. Chen, P.J. Ferreira, W. Sheng, N. Yabuuchi, L.F. Allard, Y. Shao-Horn, Enhanced Activity for Oxygen Reduction Reaction on "Pt_3Co" Nanoparticles: Direct Evidence of Percolated and Sandwich-Segregation Structures, J. Am. Soc. Brew. Chem. 130 (2008) 13818–13819.
[40] E. Lee, J.-H. Jang, A.Md. Matin, Y.-U. Kwon, One-step sonochemical syntheses of Ni@Pt core–Shell nanoparticles with controlled shape and shell thickness for fuel cell electrocatalyst, Ultrason. Sonochem. 21 (2014) 317–323.
[41] E. Lee, Y.-U. Kwon, Multi-component electrocatalyst for low-temperature fuel cells synthesized via sonochemical reactions, Ultrason. Sonochem. 29 (2016) 401–412.
[42] J.K. Nørskov, J. Rossmeisl, A. Logadottir, L. Lundkvist, J.R. Kitchin, T. Bligaard, H. Jónsson, Origin of the overpotential for oxygen reduction at a fuel-cell cathode, J. Phys. Chem. B 108 (2004) 17886–17892.
[43] F. Calle-Vallejo, D. Loffreda, M.T.M. Koper, P. Sautet, Introducing structural sensitivity into adsorption–Energy scaling relations by means of coordination numbers, Nat. Chem. 7 (2015) 403–410.
[44] F. Abild-Pedersen, Computational catalyst screening: scaling, Bond-Order and catalysis, Catal. Today 272 (2016) 6–13.
[45] P.C. Jennings, H.A. Aleksandrov, K.M. Neyman, R. Johnston, A DFT study of oxygen dissociation on platinum based nanoparticles, Nanoscale 6 (2014) 1153–1165.
[46] T.H. Yu, T. Hofmann, Y. Sha, B.V. Merinov, D.J. Myers, C. Heske, W.A. Goddard III, Finding correlations of the oxygen reduction reaction activity of transition metal catalysts with parameters obtained from quantum mechanics, J. Phys. Chem. C 117 (2013) 26598–26607.
[47] Y. Xu, A.V. Ruban, M. Mavrikakis, Adsorption and dissociation of O_2 on $Pt-Co$ and $Pt-Fe$ alloys, J. Am. Soc. Brew. Chem. 126 (2004) 4717–4725.
[48] F. Calle-Vallejo, J. Tymoczko, V. Colic, Q.H. Vu, M.D. Pohl, K. Morgenstern, D. Loffrada, P. Sautet, W. Schumann, A.S. Bandarenka, Finding optimal surface sites on heterogeneous catalysts by counting nearest neighbors, Science 350 (2015) 185–189.
[49] B.C. Han, C.R. Miranda, G. Ceder, Effect of particle size and surface structure on adsorption of O and OH on platinum nanoparticles: a first-principles study, Phys. Rev. B 77 (2008) 075410.
[50] J. Zhang, Y. Mo, M.B. Vukmirovic, R. Klie, K. Sasaki, R.R. Adzic, Platinum monolayer electrocatalysts for O_2 reduction: Pt monolayer on Pd(111) and on carbon-supported Pd nanoparticles, J. Phys. Chem. B 108 (2004) 10955–10964.
[51] L. Brewer, Bonding and structures of transition metals, Science 161 (1968) 115–122.
[52] D. Hobbs, J. Hafner, D. Spišák, Understanding the complex metallic element Mn. I. Crystalline and noncollinear magnetic structure of α-Mn, Phys. Rev. B 68 (2003) 014407.
[53] J. Hafner, D. Hobbs, Understanding the complex metallic element Mn. II. Geometric frustration in β-Mn, phase stability, and phase transitions, Phys. Rev. B 68 (2003) 014408.